Electronic quantum coherence encoded in temporal structures of N_2^+ lasing

Jinming Chen [1,4,5] Jinping Yao [1,2,*] Zhihao Zhang,[1,4,5] Zhaoxiang Liu,[1,4] Bo Xu,[1,4] Yuexin Wan,[1,4] Fangbo Zhang,[1,4]
Wei Chu [3] Lingling Qiao,[1,2] Haisu Zhang,[3] Zhenhua Wang [3] and Ya Cheng [1,2,3,6,†]

[1]*State Key Laboratory of High Field Laser Physics, Shanghai Institute of Optics and Fine Mechanics,*
Chinese Academy of Sciences, Shanghai 201800, China
[2]*CAS Center for Excellence in Ultra-intense Laser Sciences, Shanghai 201800, China*
[3]*State Key Laboratory of Precision Spectroscopy, East China Normal University, Shanghai 200062, China*
[4]*University of Chinese Academy of Sciences, Beijing 100049, China*
[5]*School of Physical Science and Technology, ShanghaiTech University, Shanghai 200031, China*
[6]*Collaborative Innovation Center of Extreme Optics, Shanxi University, Taiyuan, Shanxi 030006, China*

We experimentally and theoretically investigate temporal structures of N_2^+ lasing at the wavelengths of 391 and 428 nm. Our results show that the resonant interaction of a femtosecond laser with N_2^+ ions with a picosecond dipole relaxation time will induce a long-lasting polarization, which exists in cases of both absorption and amplification of the external seed. The induced polarization will be amplified in population-inverted N_2^+ ions, giving rise to the retarded radiation (i.e., N_2^+ lasing). The temporal profile of the retarded radiation is closely related to the dipole relaxation time, population inversion density, and propagation length. The combined experimental and theoretical study reveals the physical origin of the retarded seed amplification in N_2^+ ions.

I. INTRODUCTION

Recently, air lasing actions induced by femtosecond or nanosecond laser pulses have gained tremendous attention [1–10]. The phenomenon opens a possibility for remote sensing due to capability of generating a high-brightness, good-directionality coherent radiation in remote atmosphere [11,12]. In addition, the gain mechanism of N_2^+ lasing cannot be well understood in the framework of strong field ionization [13,14], which extends the territory of strong field molecular physics. Although there is still a hot debate on whether there is population inversion between the $B\,^2\Sigma_u^+$ and $X\,^2\Sigma_g^+$ states of N_2^+ ions [15–25], a series of studies have confirmed the key contribution of resonant excitation from the $X\,^2\Sigma_g^+$ to $A\,^2\Pi_u$ state to the generation of N_2^+ lasing [15,16,25–30]. The resonant interaction of a laser field with N_2^+ ions not only results in population redistribution among multiple electronic states, but also inevitably induces electronic coherence. Quantum coherence in N_2^+ lasing has been emphasized in recent studies [25,31–38]. For example, one has realized subcycle control of N_2^+ lasing using a pair of 800 nm (400 nm) laser pulses to manipulate quantum coherence between the $X\,^2\Sigma_g^+$ and $A\,^2\Pi_u$ $(B\,^2\Sigma_u^+)$ states [25,33,34]. The role of electronic coherence has also been clearly revealed by observing a dramatic enhancement of N_2^+ lasing with two temporally separated pump lasers [35].

Electronic coherence not only plays a vital role in the gain of N_2^+ lasing, but also influences basic properties of N_2^+ lasing. When N_2^+ lasing was observed by injecting an external seed into N_2^+ ions produced by the 800 nm pump laser in 2013 [8], it was found that the amplified lasing signal lags behind the seed pulse. The delayed radiation seems to contradict general understanding on seed amplification. Liu *et al.* [17] and Li *et al.* [39] carried out quantitative studies on the retarded lasing radiation, and demonstrated its super-radiance signatures. These works clearly reveal that the counterintuitive characteristic of N_2^+ lasing in the temporal domain is the result of quantum coherence. Nevertheless, the physical origin of the retarded radiation has not been fully understood, which motivates us to perform a combined experimental and theoretical study. In this work, we experimentally compared the temporal structures of the absorbed or amplified seed pulses at two typical N_2^+ lasing wavelengths (i.e., 391.4 and 427.8 nm). Theoretically, by solving the Maxwell-Bloch equations, we analyzed the influences of the dipole relaxation time, population inversion density, and propagation distance on the temporal profile of N_2^+ lasing. It is revealed that the retarded radiation mainly originates from the temporal mismatch between the seed pulse duration and dipole relaxation time. The former is of the order of femtoseconds, whereas the latter is of the order of picoseconds. Thus, the long-lasting polarization induced by the resonant seed light at the early stage can continue to be amplified in further propagation, giving rise to a retarded radiation. The delay of the lasing radiation with respect to the seed pulse will be shortened with the increase of population inversion density and propagation length.

II. EXPERIMENTAL SETUP

The experimental setup was illustrated in Fig. 1. A commercial Ti:sapphire laser (Legend Elite-Duo, Coherent, Inc.), which delivers 6 mJ, 800 nm, ∼40 fs laser pulses, was split

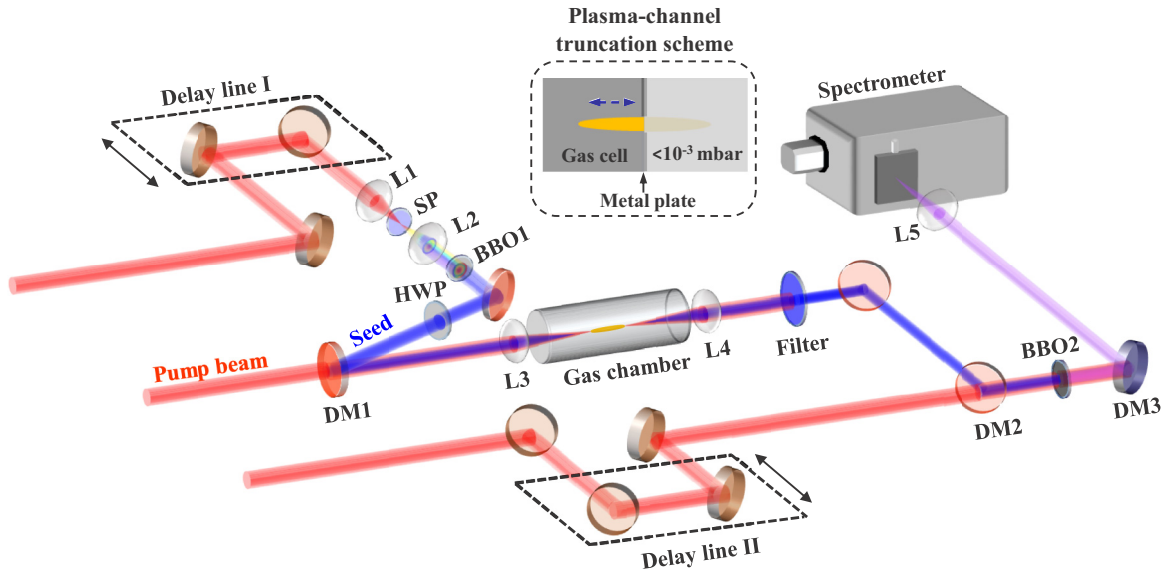*jinpingmrg@163.com
†ya.cheng@siom.ac.cn

FIG. 1. Schematic diagram of the experimental setup. DM1, DM2: dichroic mirror with high reflectivity around 400 nm and high transmission around 800 nm; DM3: dichroic mirror with high reflectivity around 266 nm and high transmission around 800 nm; HWP: half-wave plate; L1: $f = 20$ cm lens; L2: $f = 10$ cm lens; L3, L4: $f = 30$ cm lens; L5: $f = 15$ cm lens; SP: sapphire plate; BBO1: β-barium borate for double frequency generation; BBO2: β-barium borate for cross-correlation measurements. The inset shows the plasma-channel truncation scheme with a pressure gradient on two sides of the gas chamber.

into three beams. The first beam with a maximum energy of 2.4 mJ was used as the pump to ionize nitrogen molecules and produce a plasma channel. The laser energy of the pump beam can be tuned by splitters with different splitting ratios. The second beam was focused by a $f = 20$ cm lens into a 4 mm thick sapphire plate to broaden its spectrum and then was collimated by a $f = 10$ cm lens. The broadened spectrum was frequency doubled by a β-barium borate (BBO) crystal. The frequency-doubling signal at either 391 or 428 nm wavelength, depending on the phase-matched angle of the BBO crystal, was used as the external seed. The polarization of the seed was adjusted to be parallel with that of the pump beam using a half-wave plate. Both beams were combined by a dichroic mirror (DM1) and collinearly focused with a $f = 30$ cm lens into a gas cell. The time delay between two beams was controlled by a motorized translation stage (Delay line I). The seed will be amplified or absorbed in the N_2^+ ions produced by the pump laser. The amplified or absorbed seed was combined with the third 800 nm laser beam to perform cross-correlation measurements. Its temporal structure was obtained by measuring the sum frequency (SF) of two beams as a function of the time delay. Finally, the SF signal was reflected by a dichroic mirror (DM3) with a high reflectivity around 266 nm and then focused into an imaging spectrometer (Shamrock 500i, Andor).

III. EXPERIMENTAL RESULTS

We first measured the spectra of 391 nm seed pulses after passing through N_2^+ ions generated by the 800 nm pump laser with different energies. The time delay between the pump and seed pulses is chosen at ~1 ps, and the gas pressure is fixed at 6 mbar. Here, the zero time delay is defined as the moment corresponding to the strongest 391 nm emission. As

shown in Fig. 2(a), when the pump energy is 0.8 mJ, some fine absorption structures appear on the broad spectrum of seed pulses. When the pump energy is 1.25 mJ, the seed pulse is amplified by two orders of magnitude at 391.4 nm wavelength, and thus a narrow-bandwidth N_2^+ lasing was observed in Fig. 2(b), which is assigned to the band head of $B \, ^2\Sigma_u^+(v' = 0) \rightarrow X \, ^2\Sigma_g^+(v = 0)$ transition. Besides strong radiation at the band-head wavelength, some discrete peaks on the blue side are attributed to R-branch rotational transitions between the $B \, ^2\Sigma_u^+(v' = 0)$ and $X \, ^2\Sigma_g^+(v = 0)$ states, as demonstrated in a previous study [40]. Further increase of the pump energy will produce stronger N_2^+ lasing around 391 nm, as illustrated in Fig. 2(c).

Furthermore, we examined the temporal profiles of the amplified or absorbed 391 nm seed pulses in the corresponding pump energies. The temporal profile of seed pulses after passing through the plasma channel in argon is used as a reference (red dot-dashed lines), due to similar ionization probability of argon atoms and nitrogen molecules [41]. The measured results at three pump energies are shown in Figs. 2(d)–2(f). In the case of 0.8 mJ pump energy, we can observe a main peak followed by a long tail in nitrogen. However, the tail completely vanishes in argon, as shown in Fig. 2(d). It means that the seed absorption at resonant wavelengths still causes the retarded radiation, and the retarded radiation is much weaker than the main peak. At two higher pump energies corresponding to the seed amplification, the retarded radiation makes a dominant contribution to the amplified lasing signal. As observed in previous works [17,29], the seed pulse is barely amplified within its duration. With the 2.4 mJ pump energy, the retarded radiation is even stronger than the injected seed pulse, as illustrated in Fig. 2(f). In addition, the delayed radiation shows some irregular oscillations. These time-resolved measurements clearly demonstrate that the seed
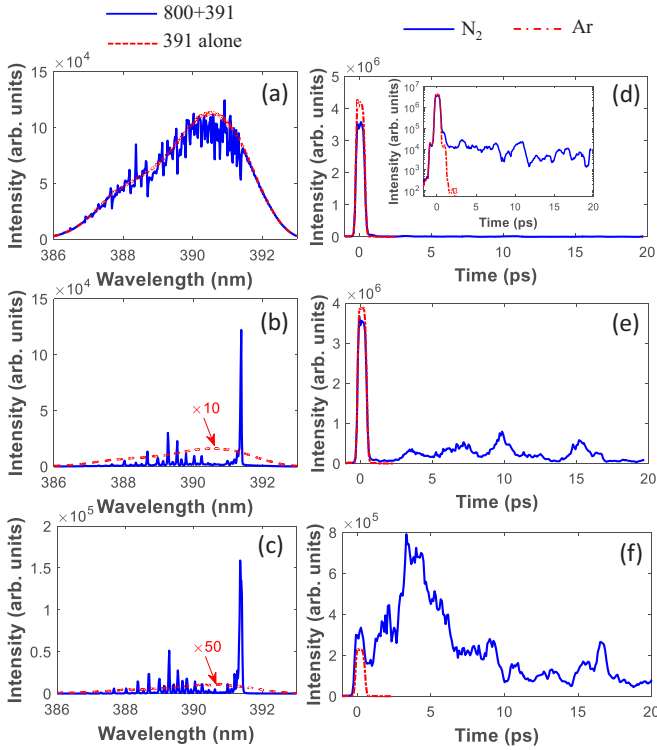
FIG. 2. The spectra of 391 nm seed pulses after passing through N_2^+ ions produced by (a) 0.8 mJ, (b) 1.25 mJ, and (c) 2.4 mJ pump laser pulses. The corresponding temporal profiles are shown in (d)–(f). For comparison, the seed spectra in the absence of the pump laser are indicated with red dashed lines, and the temporal profiles of seed pulses after passing through the plasma channel of argon are shown with red dash-dot lines. For clarity, (d) is illustrated with the logarithmic scale in the inset.

FIG. 3. Same measurements as in Fig. 2 but the seed wavelength is tuned to 428 nm and gas pressure is taken as 20 mbar.

amplification mainly occurs after the seed pulse. In addition, the retarded radiation can last a longer time as compared to the seed pulse. As a result, the N_2^+ lasing exhibits a narrow-bandwidth spectrum.

We performed the same measurement with a 428 nm external seed. The gas pressure is taken as 20 mbar to obtain strong 428 nm lasing radiation, which is assigned to the $B\ ^2\Sigma_u^+(v'=0) \rightarrow X\ ^2\Sigma_g^+(v=1)$ transition. Unlike 391 nm radiation, only amplification is observed at 428 nm at the three pump energies, as shown in Figs. 3(a)–3(c). The lower threshold for the 428 nm seed amplification can be attributed to a small population in the $X\ ^2\Sigma_g^+(v=1)$ state, which allows us to easily establish population inversion between the $B\ ^2\Sigma_u^+(v'=0)$ and $X\ ^2\Sigma_g^+(v=1)$ states [28]. Similar to 391 nm radiation, the 428 nm radiation is enhanced by increasing the pump energy. The temporal profiles of the 428 nm signals obtained at three pump energies are shown in Figs. 3(d)–3(f). Even though the absorption at 391 nm is turned into the weak amplification at 428 nm in the case of 0.8 mJ pump energy, similar retarded radiation is observed at the two wavelengths. With the increase of the pump energy, the delayed radiation gradually becomes stronger. The main features of the 428 nm radiation in the temporal domain are similar to the 391 nm radiation, but the 428 nm radiation
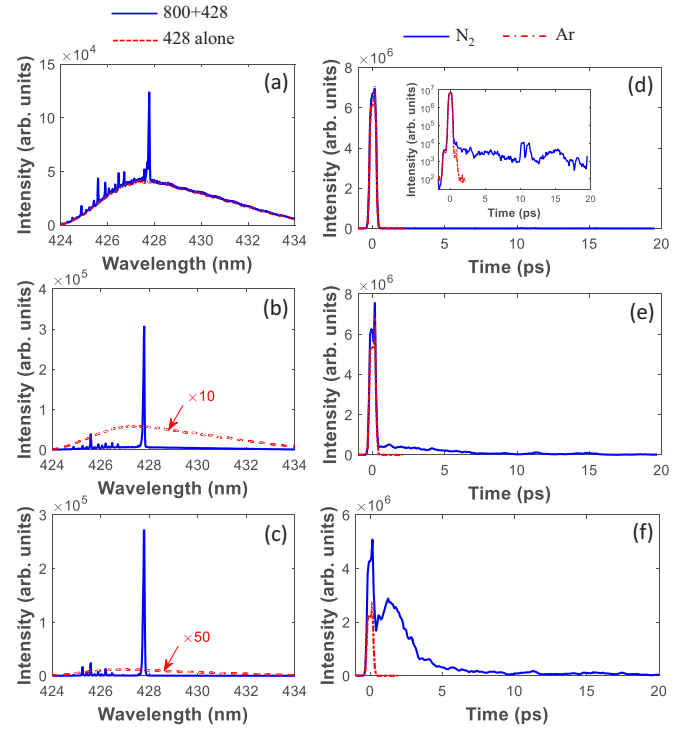
produced by the 2.4 mJ pump laser shows a smaller delay with respect to the seed pulse and a shorter duration.

We also examined the spectral and temporal evolution of 428 nm lasing radiation as a function of the propagation length at the pump energy of 2.4 mJ. In this experiment, we placed a 0.5 mm thick metal plate near the focus. The laser-drilled pinhole allows us to truncate the plasma channel through forming a pressure gradient on two sides of the pinhole, as shown in the inset of Fig. 1. The length of gain medium can be continually changed by adjusting the distance between the focal lens and the pinhole. Although the plasma channel usually shows a nonuniform distribution in the propagation path, the influence has been minimized by the choice of the measured region. As shown in Fig. 4(a), the 428 nm radiation quickly grows and then tends to saturation with the increasing propagation length. The result indicates that the 428 nm radiation has entered the saturated amplification regime. The evolution of temporal profiles with the propagation length is illustrated in Fig. 4(b). Within the seed pulse duration (i.e., main peak around zero delay), the radiation was slightly amplified along the propagation direction. In contrast, the radiation lagging behind the seed pulse exhibits a striking change during propagation. At the starting position of the lasing radiation, the retarded radiation is very weak and lasts for a long time. With the increase of propagation distance, the retarded radiation shows a higher intensity, a shorter duration, and a smaller delay with respect to the seed pulse.

IV. SIMULATION RESULTS AND DISCUSSION

To reveal the physical origin of these abnormal temporal profiles, we theoretically investigated the resonant interaction
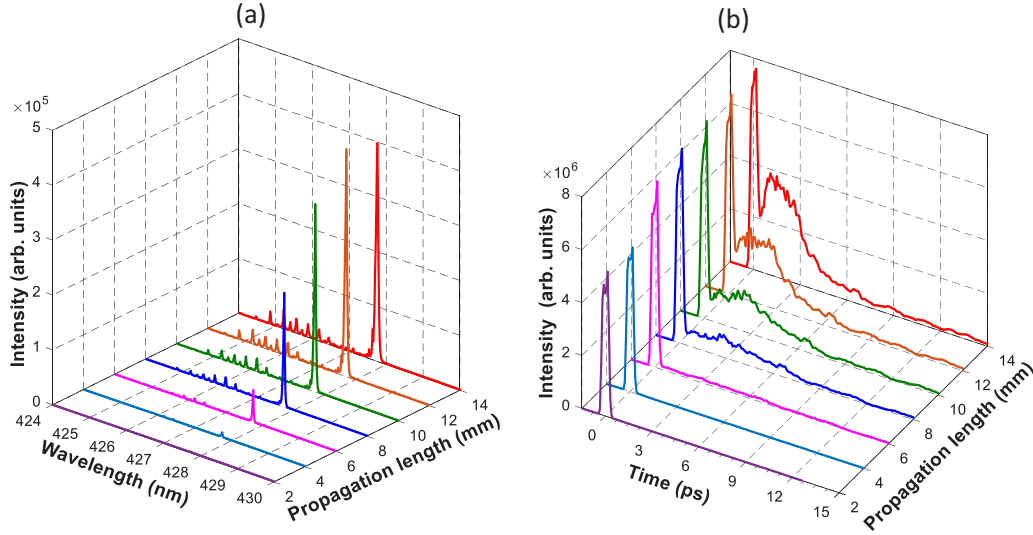
FIG. 4. (a) Spectral and (b) temporal evolution of 428 nm lasing radiation as a function of the propagation length.

of seed laser pulses with ions based on Maxwell-Bloch equations. For the sake of simplicity, two energy states of N_2^+ ions, i.e., $X\ ^2\Sigma_g^+(v = 0)$ or $X\ ^2\Sigma_g^+(v = 1)$ and $B\ ^2\Sigma_u^+(v' = 0)$ (abbreviated as X and B), are taken into consideration. It is noteworthy that although the rotational coherence makes the non-negligible contribution to the gain of N_2^+ lasing [20,40], we did not include rotational quantum states in our model considering that the pursuit of quantification of the total gain is not the primary goal of the current study. We are dedicated to unraveling the relations of electronic coherence to the retarded emission of N_2^+ lasing. As demonstrate below, the simplified model allows us to unravel the physical mechanism underlying the complicated time profiles of N_2^+ lasing.

The parameters of incident light are chosen according to the experimental conditions (i.e., peak intensity of 1×10^8 W/cm^2, pulse duration of 100 fs, and central wavelength of 391 nm or 428 nm). The peak intensity is estimated by the nJ energy, the 100 fs pulse duration, and the 100 μm focal spot. Let n_X and n_B denote the population probabilities of N_2^+ ions in the $X\ ^2\Sigma_g^+$ ($v = 0$ or $v = 1$) state and the $B\ ^2\Sigma_u^+(v' = 0)$ state, with $n_X + n_B = 1$. Since N_2^+ ions induced by strong field ionization occurs within the focal volume, the distribution of N_2^+ ions can be considered as a column with a high aspect ratio. Thus we use the paraxial one-dimensional (1D) Maxwell equation as [42]

$$\frac{\partial^2 \varepsilon}{\partial z^2} - \frac{1}{c^2}\frac{\partial^2 \varepsilon}{\partial t^2} = \mu_0 \frac{\partial^2 p}{\partial t^2}, \qquad (1)$$

where ε is the electric field and p the induced polarization in the medium, μ_0 the vacuum permeability and c the speed of light in vacuum. The electric field and induced polarization can be expressed as $\varepsilon(z,t) = 1/2E(z,t)e^{i(kz-\omega_0 t)} + $ c.c. and $p(z,t) = 1/2P(z,t)e^{i(kz-\omega_0 t)} + $ c.c. with ω_0 the central angular frequency of incident light and $k = \omega_0/c$ the wave number. In the slowly varying envelope approximation, Eq. (1) can be simplified as [43]

$$\frac{\partial E(z,t)}{\partial z} + \frac{1}{c}\frac{\partial E(z,t)}{\partial t} = \frac{i\pi}{\epsilon_0\lambda_0}P(z,t), \qquad (2)$$

where ϵ_0 is the vacuum permittivity and λ_0 the central wavelength of the incident light. By defining the retarded time $\tau = t - z/c$, Eq. (2) can be written as

$$\frac{\partial E(z,\tau)}{\partial z} = \frac{i\pi}{\epsilon_0\lambda_0}P(z,\tau). \qquad (3)$$

To obtain the induced polarization in the medium, we use the Liouville-von Neumann equation in the interaction picture as [44,45]

$$\frac{d\rho(t)}{dt} = -\frac{i}{\hbar}[H_I(t), \rho(t)] + \left(\frac{d\rho(t)}{dt}\right)_{\text{Coll}}, \qquad (4)$$

where $\rho(t)$ is the density matrix casting in the two-level system, H_I is the interaction Hamiltonian written as

$$H_I = \varepsilon(t)\begin{bmatrix} 0 & \mu e^{-i\omega_s t} \\ \mu e^{i\omega_s t} & 0 \end{bmatrix}, \qquad (5)$$

where μ is the effective dipole moment between the X and B states, ω_s is the angular frequency of B-X transition. Since the nuclear motion is frozen, μ can be approximated as $\mu = \mu_{eq}\cos\theta$ where μ_{eq} is the strength of the transition dipole moment at equilibrium nuclear distances [15] and θ is the relative angle between the molecular axis and the electric field direction ($\theta = 45°$ in this work). In addition, the collisional dissipation of the medium is phenomenologically included in $\left(\frac{d\rho(t)}{dt}\right)_{\text{Coll}}$ as $\frac{d\rho_{ii}}{dt} = -\frac{\rho_{ii}}{T_1}$ and $\frac{d\rho_{ij}}{dt} = -\frac{\rho_{ij}}{T_2}$ ($i, j = 1, 2, i \neq j$), with T_1 and T_2 being the population relaxation time and the dipole relaxation time, respectively, which are much longer than the incident pulse duration. The induced polarization $p(t)$ is given by

$$p(t) = -N\mu(\rho_{21}e^{-i\omega_s t} + \text{c.c.}), \qquad (6)$$

where N is the number density of N_2^+ ions.

With this model, we first investigated the influence of the dipole relaxation time T_2 on the temporal profile of N_2^+ lasing. With a given propagation length (i.e., 12 mm), $n_X = 0.2$, $n_B = 0.8$, and $T_1 = 500$ ps, we calculated the spectral and temporal profiles of 391 nm radiation in two cases of $T_2 = 1$ ps and $T_2 = 20$ ps. In the case of $T_2 = 1$ ps, the seed
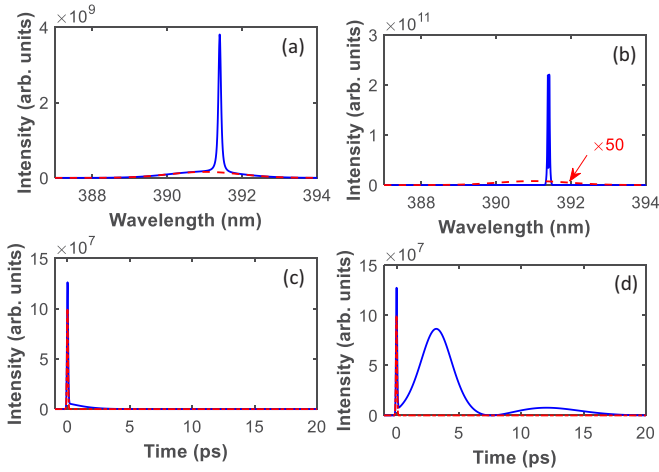
FIG. 5. The simulated spectra of 391 nm radiation with (a) $T_2 = 1$ ps and (b) $T_2 = 20$ ps. The corresponding temporal profiles are shown in (c), (d). For comparison, the initial seed spectra and the temporal profiles are indicated with red dashed lines and red dash-dot lines, respectively.

FIG. 6. The simulated spectra of 391 nm radiation with different initial population probabilities of (a) $n_X = 0.55$, $n_B = 0.45$, (b) $n_X = 0.4$, $n_B = 0.6$. The corresponding temporal profiles are shown in (c), (d). For clarity, (c) is shown with the logarithmic scale in the inset.

pulse is amplified due to the presence of population inversion, as shown in Fig. 5(a). In the temporal domain, the seed pulse is mainly amplified within its initial pulse duration, and retarded radiation exhibits a fast decay, as shown in Fig. 5(c). However, when T_2 is increased to 20 ps, which is much longer than the pulse duration of the incident seed, we can see a stronger amplification and spectral splitting around the resonant wavelength, as shown in Fig. 5(b). In this case, a strong retarded radiation and obvious oscillations are observed, as illustrated in Fig. 5(d). The comparative results clearly demonstrate that T_2 is a key factor which affects the temporal profile of N_2^+ lasing. When T_2 is much longer than the seed pulse duration, the retarded radiation can be amplified more efficiently in gain medium with a slow-decaying population inversion, resulting in the delayed amplified radiation.

We further calculated the spectral and temporal profiles of 391 nm radiation with different initial population probabilities. In the simulation, the propagation length and T_2 were fixed at 12 mm and 20 ps, respectively. In the absence of population inversion as shown in Figs. 6(a) and 6(c), the initial seed pulse is attenuated in the spectral and temporal domain within its pulse duration. However, the resonant interaction of seed pulses with the medium induces the long-lasting and slow-decaying polarization, which results in the retarded radiation after the seed pulse, as illustrated in Fig. 6(c). When the population inversion is established, as shown in Figs. 6(b) and 6(d), the incident pulse can be strongly amplified at ~391 nm and the retarded radiation becomes remarkable. In addition, the retarded radiation reaches the maximum around 10 ps after the seed pulse. As shown in Fig. 5(d), higher population inversion density results in the stronger retarded radiation as well as the shift of its temporal profile towards the incident seed pulse. Therefore, simulation results reproduce the main trends and characteristics of the experimental results.

For comparison, we also calculated spectral and temporal profiles of the 428 nm radiation in different initial population
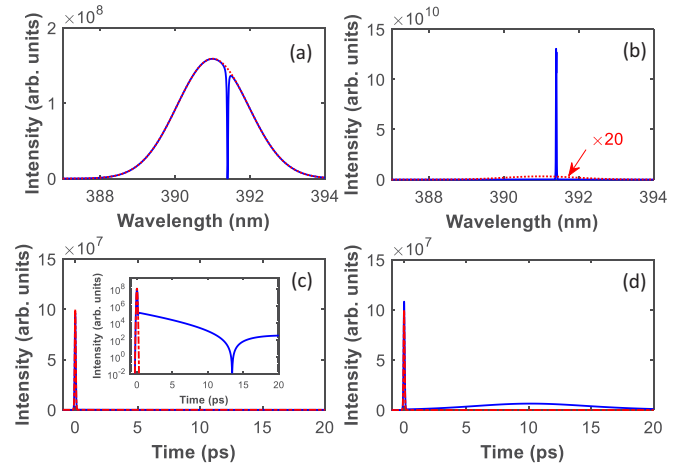
probabilities but with a shorter dipole relaxation time (i.e., $T_2 = 5$ ps) due to the higher collision rate for the higher pressure, as shown in Fig. 7. Due to the smaller population in the $X\,^2\Sigma_g^+ (v = 1)$ state than that in the $X\,^2\Sigma_g^+ (v = 0)$ state, we choose the higher population inversion density in the calculation of the 428 nm radiation. As expected, the increase of the population inversion density causes the retarded radiation with a higher intensity, a shorter pulse duration, and a smaller delay with respect to the initial seed.

We further calculated the spectral and temporal evolution of 428 nm radiation as a function of the propagation length L with $n_X = 0.15$, $n_B = 0.85$, and $T_2 = 5$ ps, as depicted in Fig. 8. As the propagation length increases, the 428 nm radiation firstly grows rapidly and then tends to saturation at $L = 10$ mm, as shown in Fig. 8(a), which agrees well with the experimental result. The temporal evolution of the 428 nm
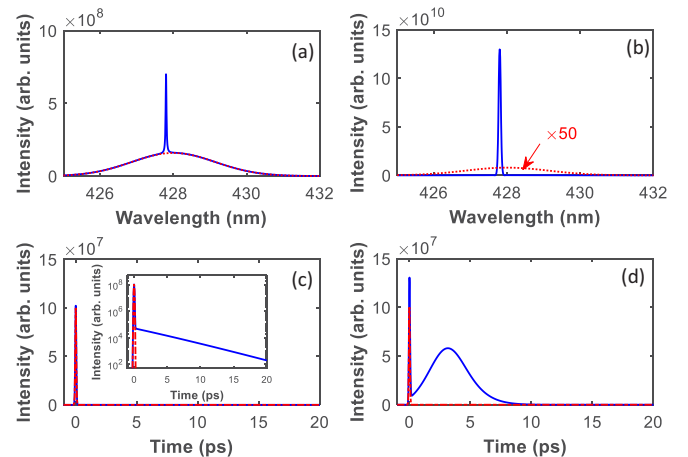

FIG. 7. The simulated spectra of 428 nm radiation in different initial population probabilities of (a) $n_X = 0.45$, $n_B = 0.55$, (b) $n_X = 0.15$, $n_B = 0.85$. The corresponding temporal profiles are shown in (c), (d). For clarity, the logarithmic scale of (c) is shown in corresponding inset.
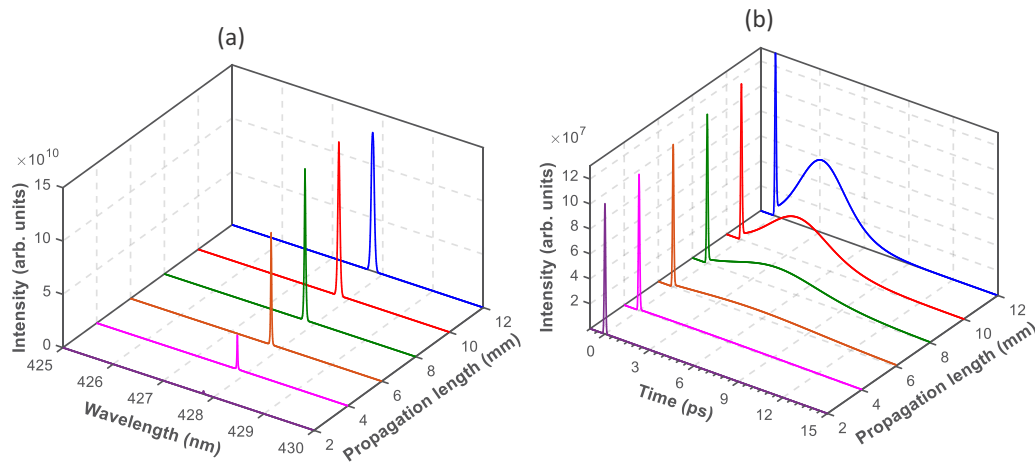
FIG. 8. (a) The simulated spectral and (b) temporal evolution of 428 nm radiation as a function of propagation length.

radiation during the propagation is illustrated in Fig. 8(b). At the initial stage of the 428 nm lasing radiation (i.e., $L = 4$ mm), a long and weak temporal profile appears after the seed pulse. With increase of the propagation length, the retarded radiation becomes stronger. At the stage of saturation amplification, further increase of L will shorten the duration of the retarded radiation and force its temporal profile to shift towards the seed pulse.

Based on the above-mentioned simulation results, we will discuss the underlying physics responsible for the retarded radiation in N_2^+ lasing. The simulation results in Figs. 5–8 clearly demonstrate that the temporal profile of N_2^+ lasing is closely related to the dipole relaxation time, the population inversion density, and the propagation length. These simulation results qualitatively reproduce the temporal characteristics of 391 and 428 nm lasing signals. Briefly speaking, the difference of 391 and 428 nm in the temporal domain can be attributed to different population inversion densities. These simulation results also reveal that the resonant interaction of the femtosecond seed pulse with N_2^+ ions will cause a slow-decaying polarization, which is determined by the dipole relaxation time or the dephasing time in the quantum system. The long-lived polarization leads to the retarded radiation at the resonant wavelengths. For the case of no gain or small gain (corresponding to the low pump energy), the retarded radiation exhibits the relatively weaker intensity and the longer duration. However, for the case of high gain (corresponding to the high pump energy), the high population inversion density enables further amplification of the retarded radiation during the propagation. When the retarded radiation is strong enough, it will in turn affect the polarization of the medium. In the regime of saturated amplification, the retarded radiation close to the seed pulse will deplete the population in the upper state and obtain the more efficient amplification. Therefore, with the increase of propagation length or population inversion

density, N_2^+ lasing radiation shows a shorter pulse duration and a smaller delay with respect to the seed pulse, as demonstrated experimentally and theoretically.

V. CONCLUSIONS

In conclusion, we reveal the physical origin of the delay of 391 and 428 nm lasing signals with respect to the seed pulse by a combined experimental and theoretical investigation. It was shown that the resonant interaction of the seed pulse with N_2^+ ions induces a long-lasting polarization after the passage of the seed pulse, which gives rise to the generation of retarded N_2^+ lasing radiations. The simulation results also display that the postponed lasing radiations are sensitive to the propagation length, population inversion density, and dipole dephasing time. Both experimental and theoretical results convince us that the retarded N_2^+ lasing mainly originates from the electronic quantum coherence induced by ultrafast lasers, which deepens the understanding of resonant interaction of femtosecond lasers with molecular ions.

[1] A. Dogariu, B. Michael, O. Scully, and B. Miles, Science **331**, 442 (2011).

[2] A. Laurain, M. Scheller, and P. Polynkin, Phys. Rev. Lett. **113**, 253901 (2014).

[3] Q. Luo, W. Liu, and S. L. Chin, Appl. Phys. B **76**, 337 (2003).

[4] S. Mitryukovskiy, Y. Liu, P. Ding, A. Houard, and A. Mysyrowicz, Opt. Express **22**, 12750 (2014).

[5] D. Kartashov, S. Ališauskas, G. Andriukaitis, A. Pugžlys, M. Shneider, A. Zheltikov, S. L. Chin, and A. Baltuška, Phys. Rev. A **86**, 033831 (2012).

[6] D. Kartashov, S. Ališauskas, A. Baltuška, A. Schmitt-Sody, W. Roach, and P. Polynkin, Phys. Rev. A **88**, 041805(R) (2013).

[7] J. Yao, B. Zeng, H. Xu, G. Li, W. Chu, J. Ni, H. Zhang, S. L. Chin, Y. Cheng, and Z. Xu, Phys. Rev. A **84**, 051802(R) (2011).

[8] J. Yao, G. Li, C. Jing, B. Zeng, W. Chu, J. Ni, H. Zhang, H. Xie, C. Zhang, H. Li, H. Xu, S. L. Chin, Y. Cheng, and Z. Xu, New J. Phys. **15**, 023046 (2013).

[9] P. Polynkin and Y. Cheng, *Air Lasing* (Springer International Publishing AG, Cham, Switzerland, 2018).

[10] J. Yao and Y. Cheng, Chin. J. Lasers **47**, 0500005 (2020).

[11] V. Kocharovsky, S. Cameron, K. Lehmann, R. Lucht, R. Miles, Y. Rostovtsev, W. Warren, R. Welch, and O. Scully, P. Natl. Acad. Sci. USA **102**, 7806 (2005).

[12] P. Malevich, R. Maurer, D. Kartashov, S. Ališauskas, A. Lanin, A. Zheltikov, M. Marangoni, G. Cerullo, A. Baltuška, and A. Pugžlys, Opt. Lett. **40**, 2469 (2015).

[13] M. Ammosov, N. Delone, and V. Krainov, Zh. Eksp. Teor. Fiz. **91**, 2008 (1986) [Sov. Phys. - JETP **64**, 1191 (1986)].

[14] X. M. Tong, Z. X. Zhao, and C. D. Lin, Phys. Rev. A **66**, 033402 (2002).

[15] J. Yao, S. Jiang, W. Chu, B. Zeng, C. Wu, R. Lu, Z. Li, H. Xie, G. Li, C. Yu, Z. Wang, H. Jiang, Q. Gong, and Y. Cheng, Phys. Rev. Lett. **116**, 143007 (2016).

[16] H. Xu, E. Lötstedt, A. Iwasaki, and K. Yamanouchi, Nat. Commun. **6**, 8347 (2015).

[17] Y. Liu, P. Ding, G. Lambert, A. Houard, V. Tikhonchuk, and A. Mysyrowicz, Phys. Rev. Lett. **115**, 133203 (2015).

[18] M. Britton, P. Laferriere, D. H. Ko, Z. Li, F. Kong, G. Brown, A. Naumov, C. Zhang, L. Arissian, and P. B. Corkum, Phys. Rev. Lett. **120**, 133208 (2018).

[19] A. Azarm, P. Corkum, and P. Polynkin, Phys. Rev. A **96**, 051401(R) (2017).

[20] D. Kartashov, S. Haessler, S. Ališauskas, G. Andriukaitis, A. Pugžlys, A. Baltuška, J. Möhring, D. Starukhin, M. Motzkus, A. M. Zheltikov, M. Richter, F. Morales, O. Smirnova, M. Y. Ivanov, and M. Spanner, in *Conference on High Intensity Lasers and High Field Phenomena* (Optical Society of America, Washington, DC, 2014), paper HTh4B.5.

[21] J. Yao, W. Chu, Z. Liu, J. Chen, B. Xu, and Y. Cheng, Appl. Phys. B **124**, 73 (2018).

[22] H. Li, Q. Song, J. Yao, Z. Liu, J. Chen, B. Xu, K. Lin, J. Qiang, B. He, H. Xu, Y. Cheng, H. Zeng, and J. Wu, Phys. Rev. A **99**, 053413 (2019).

[23] W. Zheng, Z. Miao, L. Zhang, Y. Wang, C. Dai, A. Zhang, H. Jiang, Q. Gong, and C. Wu, J. Phys. Chem. Lett. **10**, 6598 (2019).

[24] Q. Zhang, H. Xie, G. Li, X. Wang, H. Lei, J. Zhao, Z. Chen, J. Yao, Y. Cheng, and Z. Zhao, Commun. Phys. **3**, 50 (2020).

[25] A. Mysyrowicz, R. Danylo, A. Houard, V. Tikhonchuk, X. Zhang, Z. Fan, Q. Liang, S. Zhuang, L. Yuan, and Y. Liu, APL Photonics **4**, 110807 (2019).

[26] H. Li, M. Hou, H. Zang, Y. Fu, E. Lötstedt, T. Ando, A. Iwasaki, K. Yamanouchi, and H. Xu, Phys. Rev. Lett. **122**, 013202 (2019).

[27] T. Ando, E. Lötstedt, A. Iwasaki, H. Li, Y. Fu, S. Wang, H. Xu, and K. Yamanouchi, Phys. Rev. Lett. **123**, 203201 (2019).

[28] B. Xu, S. Jiang, J. Yao, J. Chen, Z. Liu, W. Chu, Y. Wan, F. Zhang, L. Qiao, R. Lu, Y. Cheng, and Z. Xu, Opt. Express **26**, 13331 (2018).

[29] X. Zhong, Z. Miao, L. Zhang, Q. Liang, M. Lei, H. Jiang, Y. Liu, Q. Gong, and C. Wu, Phys. Rev. A **96**, 043422 (2017).

[30] H. Xie, Q. Zhang, G. Li, X. Wang, L. Wang, Z. Chen, H. Lei, and Z. Zhao, Phys. Rev. A **100**, 053419 (2019).

[31] Z. Liu, J. Yao, J. Chen, B. Xu, W. Chu, and Y. Cheng, Phys. Rev. Lett. **120**, 083205 (2018).

[32] J. Yao, W. Chu, Z. Liu, B. Xu, J. Chen, and Y. Cheng, New J. Phys. **20**, 033035 (2018).

[33] A. Zhang, Q. Liang, M. Lei, L. Yuan, Y. Liu, Z. Fan, X. Zhang, S. Zhuang, C. Wu, Q. Gong, and H. Jiang, Opt. Express **27**, 12638 (2019).

[34] A. Zhang, M. Lei, J. Gao, C. Wu, Q. Gong, and H. Jiang, Opt. Express **27**, 14922 (2019).

[35] J. Chen, J. Yao, H. Zhang, Z. Liu, B. Xu, W. Chu, L. Qiao, Z. Wang, J. Fatome, O. Faucher, C. Wu, and Y. Cheng, Phys. Rev. A **100**, 031402(R) (2019).

[36] L. Yuan, J. Yao, Y. Liu, and Y. Cheng, Adv. Quantum Technol. **2**, 1900080 (2019).

[37] J. Chen, J. Yao, Z. Liu, B. Xu, F. Zhang, Y. Wan, W. Chu, Z. Wang, L. Qiao, and Y. Cheng, Chin. Phys. Lett. **36**, 104204 (2019).

[38] H. Xie, H. Lei, G. Li, Q. Zhang, X. Wang, J. Zhao, Z. Chen, J. Yao, Y. Cheng, and Z. Zhao, Phys. Rev. Res. **2**, 023329 (2020).

[39] G. Li, C. Jing, B. Zeng, H. Xie, J. Yao, W. Chu, J. Ni, H. Zhang, H. Xu, Y. Cheng, and Z. Xu, Phys. Rev. A **89**, 033833 (2014).

[40] H. Zhang, C. Jing, J. Yao, G. Li, B. Zeng, W. Chu, J. Ni, H. Xie, H. Xu, S. L. Chin, K. Yamanouchi, Y. Cheng, and Z. Xu, Phys. Rev. X **3**, 041009 (2013).

[41] Z. Y. Lin, X. Y. Jia, C. L. Wang, Z. L. Hu, H. P. Kang, W. Quan, X. Y. Lai, X. J. Liu, J. Chen, B. Zeng, W. Chu, J. P. Yao, Y. Cheng, and Z. Z. Xu, Phys. Rev. Lett. **108**, 223001 (2012).

[42] A. Icsevgi and W. E. Lamb, Phys. Rev. **185**, 517 (1969).

[43] F. A. Hopf and M. O. Scully, Phys. Rev. **179**, 399 (1969).

[44] Th. Vieillard, F. Chaussard, F. Billard, D. Sugny, O. Faucher, S. Ivanov, J.-M. Hartmann, C. Boulet, and B. Lavorel, Phys. Rev. A **87**, 023409 (2013).

[45] S. Ramakrishna and T. Seideman, J. Chem. Phys. **124**, 034101 (2006).